Solar Energy Materials & Solar Cells 306 (2026) 114514

Contents lists available at ScienceDirect

Solar Energy Materials and Solar Cells

journal homepage: www.elsevier.com/locate/solmat

Computational study of intrinsic defects and photoluminescence spectra in CdTe

M. Sitaula [a], V.T. Barone [a], B. K C [a], B.R. Tuttle [b], R.J. Ellingson [a], S.V. Khare [a,*]

[a] Department of Physics and Astronomy, and Wright Center for Photovoltaics Innovation and Commercialization (PVIC), University of Toledo, Toledo, OH, 43606, USA
[b] Department of Physics, Penn State Behrend, Erie, PA, 16563, USA

ARTICLE INFO

Keywords:
CdTe
Electron-phonon coupling
Point defects
Density functional theory
First principles
Defect formation energies
PL spectra

ABSTRACT

First-principles modeling of photoluminescence (PL) line shapes of defect systems is emerging as an important tool for identifying optically active centers in semiconductors. We examine the structural, electronic, and optical properties of intrinsic point defects (V_{Cd}, V_{Te}, Cd_{Te}, and Te_{Cd}) in CdTe using density functional theory (DFT) and beyond methods. The calculated defect formation energies for the 216-atom supercell, ranging from 0.817 to 5.651 eV in different charge states, are plotted within the band gap to evaluate stability. Vacancies and antisites are identified as the most prevalent native defects. The band structures and total density of states calculations demonstrate that the presence of defects perturbs the electronic structure, leading to localized states near the Fermi level. In addition, shifts of the band extrema to different *k*-points indicate slight variations in the band gap, which remains nearly zero in most cases. The calculated PL spectra and Huang-Rhys Factor (S) for the stable defect states (V_{Te}^{0}, V_{Te}^{2+}, V_{Cd}^{0}, Te_{Cd}^{0}, and Cd_{Te}^{2+}) are predictive of defect-induced optical transitions. Our results revealed that neutral vacancy defects exhibit sharp, zero phonon line (ZPL) dominated emission due to weak electron-phonon coupling ($S = 0.0024$). In contrast, antisite defects introduce deep transition levels, leading to strong electron phonon interactions and characteristically broad, Gaussian-like PL spectra with high spectral value ($S = 100.07$). This work provides insights into the electrical properties, defect energetics, and PL spectra of intrinsic point defects that could predict the experimental photoluminescence observations in CdTe.

1. Introduction

Cadmium telluride (CdTe) is a semiconductor of significant interest for photovoltaic applications, primarily due to its nearly optimal direct band gap (1.5 eV) and its suitability for low-cost, ease of manufacturing [1,2]. Despite these advantages, device performance remains heavily contingent upon the material's chemistry. Specifically, point defects play a decisive role in governing the electronic and optical properties of CdTe by influencing doping efficiency, charge compensation, carrier recombination, and phase stability [3,4]. While experimental identification of these defects is often challenging and indirect, typically requiring an ingenious combination of multiple techniques. First principles calculations have emerged as a powerful complementary approach and have become sufficiently reliable to serve as a predictive tool for understanding and engineering defect behavior in semiconductor-based devices [5,6]. Furthermore, computational evaluations of passivation strategies for deep-level defects are also becoming important for improving device efficiency and advancing the development of emerging photovoltaic materials [7].

The properties and performance of most functional materials and devices are controlled by their defect structures [8,9]. Despite over seven decades of experimental and theoretical research [10–14], the defect chemistry is still not well understood. The atomistic origins of many experimentally observed spectroscopic signatures remain unclear [15]. A thorough understanding of defect behavior is therefore essential for mitigating their detrimental effects on device performance [16–19]. Achieving this understanding through modeling is a vital computational requirement for ensuring the reliability of these insights.

The supercell approach is widely used to study point defects in solids [20,21]. Specifically, when supercells are treated under periodic boundary conditions, the total energies of charged defects are often inaccurately estimated due to spurious electrostatic interactions between the defect, its periodic images, and the compensating background charge [22–24]. Additionally, strong finite-size effects in smaller cells may severely distort the conduction band, rendering band gap corrections and formation energies for negatively charged defects unreliable

* Corresponding author.
E-mail address: sanjay.khare@utoledo.edu (S.V. Khare).

https://doi.org/10.1016/j.solmat.2026.114514
Received 14 March 2026; Received in revised form 11 June 2026; Accepted 12 June 2026
Available online 26 June 2026

and incompatible with the dilute defect limit [25]. To address these inaccuracies and ensure converged defect energetics, we employ a 64-atom supercell (SC64), typically constructed as a $2 \times 2 \times 2$ expansion of the 8-atom cubic unit cell and a larger 216-atom supercell (SC216), derived from a $3 \times 3 \times 3$ expansion of the primitive cell. These supercells have a cubic symmetry, relatively large defect-image separation, and computational affordability for methods beyond DFT [26–30]. Furthermore, we employ the Freysoldt-Neugebauer-Van de Walle (FNV) scheme to correct for electrostatic image interactions and potential alignment [22,24]. By applying these finite-size corrections across varying supercell sizes, we could minimize artifacts and provide a robust analysis of defect-induced photoluminescence.

PL spectroscopy is widely used to probe the optoelectronic properties of point defects, yielding information about excitation energies and the interaction of excited electronic states with lattice vibrations [31]. The electronic excitation of point defects couples strongly to lattice vibrations, making electron-phonon interactions central to understanding their optical signatures. These excitations induce localized lattice relaxation, leading to electron-phonon coupling that governs key characteristics such as PL intensity, spectral broadening, and the presence of zero-phonon lines [32,33].

A rigorous theoretical description of defect luminescence remains challenging, as point defects break the translational symmetry of the host lattice and involve many coupled electronic and vibrational degree of freedom [34]. This is typically addressed using the Huang-Rhys (HR) configuration coordination framework, which reduces the multidimensional vibrational problem into a single collective coordinate. This model enables the quantitative evaluation of electron phonon coupling via the HR factor S(ω) [32,35]. Within this framework, first-principles calculations based on density functional theory (DFT), combined with vibrational analysis, have become powerful tools for predicting defect formation energies, charge-state transition levels, and optical emission properties in semiconductors [5,36–38]. Such calculations provide deep microscopic insight into defect stability and luminescence mechanisms, facilitating a consistent interpretation of experimental PL spectra and guiding future defect engineering strategies [12].

In this study, we present a comprehensive analysis of the electronic properties, intrinsic point defects, and PL spectra of cubic CdTe using density functional theory and beyond. We calculated the lattice constants, band gap, band structures, density of states, and formation energy plots for defects including vacancies and antisites. Moreover, PL spectra were simulated using 64 atom supercells to examine the defect-induced optical transitions and electron-phonon coupling.

Under typical growth conditions, we find that vacancies and antisites are the most prevalent defects. Formation energy calculations further indicate that shallow defects predominate across various charge states. Electronic properties analysis demonstrates that the introduction of native defects significantly perturbs the host crystal lattice, fundamentally altering its macroscopic properties. Furthermore, PL spectra simulations reveal that neutral vacancy defects exhibit sharp, zero phonon line (ZPL) dominated emissions due to weak electron-phonon coupling. In contrast, antisite defects introduce deep transition levels, resulting in strong electron phonon interactions and broad PL spectra. This work provides a rigorous theoretical reference for future experimental investigations into point defects and the optical characterization of CdTe.

2. Computational methods

The density functional theory (DFT) and beyond computations were conducted using the Vienna Ab initio Simulation Package (VASP [30, 39–43]). The Perdew-Burke-Ernzerhof (PBE) [44–47] generalized gradient approximation (GGA) exchange-correlation functional was employed in the projector augmented wave (PAW) method [48–52]. Standard PAW potentials were used to represent the core-electrons, and the valence electrons included were ($4d^{10}5s^2$) and ($5s^25p^4$) for cadmium (Cd) and tellurium (Te), respectively. To achieve a more accurate band gap, we used the Heyd-Scuseria-Ernzerhof (HSE06) hybrid functional [53–56]. Defect calculations were carried out using the semi-local approximation exchange-correction functional (PBEsol) [57], optimized for solids, in conjunction with the pydefect [58] software package. The PBEsol functional provides a lower computational cost compared to HSE06, enabling defect studies with larger supercells while maintaining reasonable accuracy. This approach also minimizes finite-size effects and allows defect calculations to be performed at a manageable computational expense. Atomic positions were relaxed until the forces reached a tolerance of 0.03 eV/Å.

To model point defects, $2 \times 2 \times 2$ (64-atom) and $3 \times 3 \times 3$ (216-atom) supercells in the zinc blende structure were constructed from the optimized primitive cell of CdTe containing 8 atoms. A plane-wave cutoff energy of 380 eV was used for all calculations. Brillouin zone integrations employed a Γ-centered $1 \times 1 \times 1$ k-point mesh for the supercell calculations. The calculated lattice constant of CdTe was 6.60 Å, in good agreement with the experimental value of 6.48 Å [59].

We studied both neutral and charged point defects, including tellurium vacancies (Va_{Te1}) with charge states 0, +1, and +2; cadmium vacancies (Va_{Cd1}) with charge states 0, –1, and –2; tellurium-on-cadmium substitutions (Te_{Cd1}) with charge states 0, –1, –2, –3, and –4; and cadmium-on-tellurium substitutions (Cd_{Te1}) with charge states 0, +1, +2, +3 and + 4. The defect formation energies were calculated using the following equation [60–63].

$$E_f[D^q] = E_{tot}[D^q] - E_{tot}[bulk] - \sum_i \mu_i n_i + q(E_F + E_{VBM} + \Delta V) + E_{corr}, \quad (1)$$

Where $E_f[D^q]$ is the formation energy of the periodic supercell for the bulk CdTe crystal with point defect [D]; $E_{tot}[D^q]$ is the total energy of the defective supercell in charge state q; $E_{tot}[bulk]$ denotes the total energy of a bulk unit cell with the same size of the defect cell; n_i is the number of atoms of species i added or removed; μ_i are the corresponding chemical potentials of these species; E_F is the electronic Fermi energy, which typically varies from 0 to the band gap value; E_{VBM} is the energy of the valence band maximum of the bulk CdTe crystal. Finally, ΔV & E_{corr} are finite-size correction terms calculated using the methods developed by Freysoldt-Neugebauer-Van de Walle (FNV) scheme [22,24] to account for electrostatic image interactions and potential alignment. The chemical potential diagram (CPD) was also constructed to determine the allowed range of elemental chemical potentials (μ_i) under Cd-rich and Te-rich conditions. Additionally, to analyze the influence of the point defects on the electronic structure, we calculated the total density of states (TDOS) and band structures for both pristine and defective supercells.

The defect formation energies were calculated using the GGA-based PBEsol functional. To account for the underestimated PBEsol band gap of CdTe, a band-edge correction (scissor operation) scheme was employed, in which the conduction band minimum (CBM) was shifted to reproduce the HSE06 band gap of 1.42 eV, while the valence band maximum was fixed at 0 eV. Accordingly, the Fermi-level range in the defect formation energy diagrams was extended to the HSE06 band gap, following widely used approaches in defect calculations [64,65].

Photoluminescence (PL) [66] spectra were calculated by post-processing outputs from VASP and Phonopy [67] to evaluate the Huang-Rhys (HR) factor S ($\hbar\omega$) [32,68] and generate PL line shapes for defect systems. At finite temperature it is expressed as [31]

$$L(\hbar\omega) \propto \omega^3 \int_{-\infty}^{\infty} dt\, G(t,T) e^{i\omega t - \frac{\lambda}{\hbar}|t| - i\frac{E_{ZPL}}{\hbar}t}, \quad (2)$$

where E_{ZPL} is the zero-phonon line energy and λ is a line shape parameter, taken as 2.5 meV at T = 50 K.

The generating function describing the electron-phonon coupling is written as

$$G(t,T) = exp\left[-\sum_k S_k\left(\left(1 - e^{i\omega_k t}\right) + \overline{n_k}(T)\left(2 - e^{i\omega_k t} - e^{-i\omega_k t}\right)\right)\right], \quad (3)$$

where S_k is the partial Huang-Rhys factor for phonon mode k, ω_k is the phonon frequency, and $\overline{n_k}$ (T) is the average occupation number of the kth phonon mode:

$$\overline{n_k}\,(T) = \frac{1}{e^{\frac{\hbar\omega_k}{k_B T}} - 1}. \quad (4)$$

where k_B is the Boltzmann constant.

In practice, Equation (3) can be written in an alternative form:

$$G(t,T) = e^{S(t) - S(0) + C(t,T) + C(-t,T) - 2C(0,T)}, \quad (5)$$

where $S(t) = \sum_k S_k e^{i\omega_k t}$ and $C(t,T) = \sum_k \overline{n_k}(T) S_k e^{i\omega_k t}$. These quantities are obtained from the Fourier transforms of the spectral densities:

$$S(\hbar\omega) = \sum_k S_k \delta(\hbar\omega - \hbar\omega_k), \quad (6)$$

$$C(\hbar\omega, T) = \sum_k \overline{n_k}(T) S_k \delta(\hbar\omega - \hbar\omega_k). \quad (7)$$

The electron-phonon coupling strength (S_k) is quantified for the mode k as the following expression [35].

$$S_k = \frac{\omega_k\, q_k^2}{2\hbar}, \quad (8)$$

where q_k is the mass-weighted displacement along the kth mode, evaluated as [32,69]:

$$q_k = \sum_{\alpha,i} \sqrt{m_\alpha}\left(R_{e,\alpha,i} - R_{g,\alpha,i}\right)\Delta r_{k,\alpha,i}, \quad (9)$$

Here, m_α is the mass of the α atom, R represents the atomic positions in both excited and ground states, and $\Delta r_{k,\alpha,i}$ is a normalized displacement vector of atom α in the direction i of phonon mode k.

Further,

$$S(t) = \int_0^\infty S\,(\hbar\omega) e^{-i\omega t} d(\hbar\omega), \quad (10)$$

and

$$S \equiv S(t=0) = \int_0^\infty S(\hbar\omega)\, d(\hbar\omega) = \sum_k S_k, \quad (11)$$

is the total HR factor for a given optical transition. The defective supercell was 64 atoms. The procedure involved fully optimizing the ground and excited state defect configurations within DFT to obtain their relaxed geometries and total energies. Phonon modes for the ground state structure were computed in the harmonic approximation using Phonopy, with force constants extracted from single-point VASP calculations on displaced atomic configurations. The excited state geometry was obtained by manually adjusting the electronic occupancies (FERWE/FERDO) [5,33] in VASP. The zero-phonon line (ZPL) [33] energy was determined as the total energy difference between the excited and ground states. Using the ground and excited state CONTCAR files along with the OUTCAR from the phonon calculations, the HR factor and the corresponding PL line-shape were computed.

3. Results

3.1. Electronic properties of bulk and defective CdTe

CdTe is a semiconductor belonging to the II-VI group that primarily crystallizes in the cubic zinc blende structure (space group $F\bar{4}3m$), as shown in Fig. 1. The calculated lattice constant is 6.604 Å, which is in reasonable agreement with the experimental value of 6.481 Å [71].

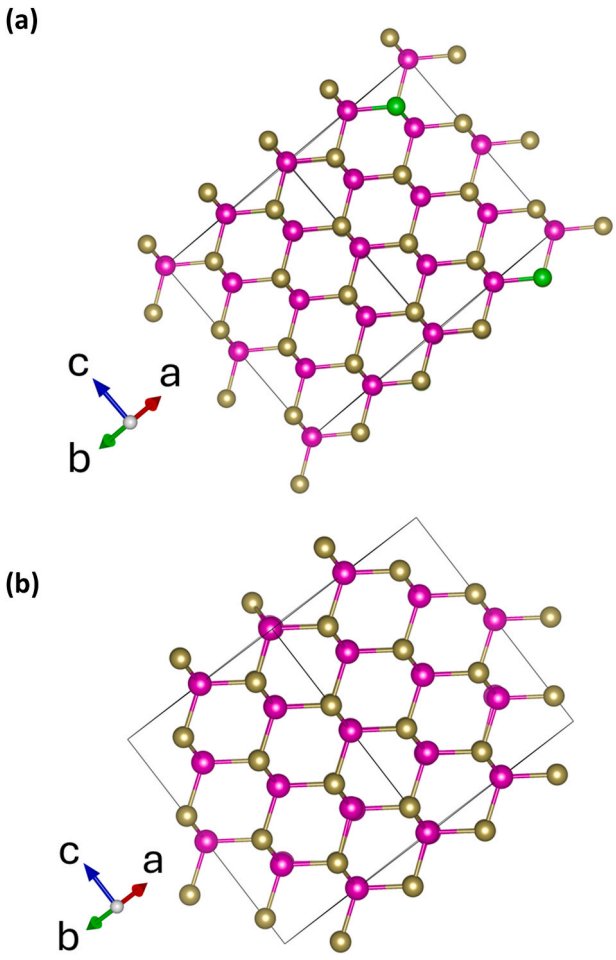

Fig. 1. Ball and stick representation of a 64-atom CdTe supercell model viewed along the crystallographic axes. The top panel **(a)** shows the pristine structure, whereas the bottom panel **(b)** displays the defected state of a tellurium vacancy (V_{Te}^0), in which a Te atom (green) has been removed. Pink and gold spheres denote cadmium and tellurium atoms, respectively, as generated using the VESTA program [70]. (For interpretation of the references to colour in this figure legend, the reader is referred to the Web version of this article.)

The calculated band structures of bulk and defective CdTe are shown in Fig. 2, where the Fermi level is set at 0 eV. From Fig. 2 (a), the band gap of bulk CdTe is 0.60 eV, which is smaller than the experimental value of 1.47 eV [72]. This underestimation mainly arises from the use of the GGA functional. Additional minor deviations may result from the treatment of electron-ion interactions and the finite basis-set expansion of the wave functions [73]. However, calculations performed using the hybrid functional (HSE06) yield a band gap of 1.42 eV, which is very close to the experimental value of 1.47 eV [72]. In addition, both the valence band maximum and the conduction band minimum are located at the Γ point, indicating that CdTe is a direct band gap semiconductor.

By introducing defects, there is a noticeable modification in the conduction-band dispersion, suggesting that these defects perturb the host electronic states rather than just forming localized levels. Similar to observations by Menendez-Proupin and Orellana [25], these changes can arise from the artificially high defect concentrations and dense k-point sampling inherent to small supercells. Additionally, finite-size effects may distort the host band edges, complicating both gap corrections and the interpretation of defect energetics. We use a 64-atom supercell for our band structure calculations. However, employing even larger supercells and reduced Brillouin-zone sampling can mitigate these artifacts, yielding a more representative description of

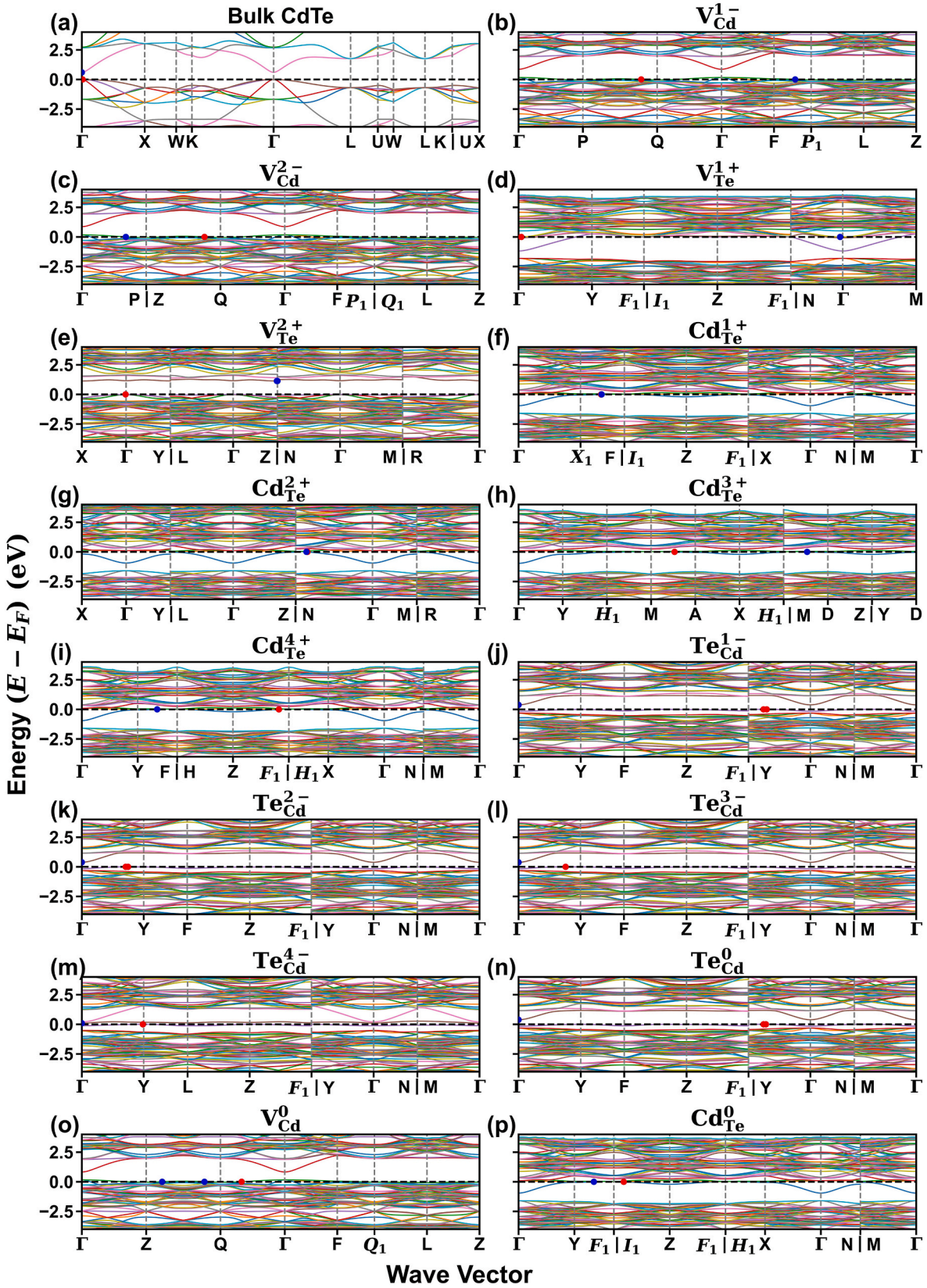

Fig. 2. The electronic band structures of CdTe plotted along high-symmetry paths in the Brillouin zone. Panel **(a)** is the 8-atom pristine cell, while panels **(b–p)** correspond to 64-atom supercell containing different defect configurations. The red and blue dots mark the valence band maximum (VBM) and conduction band minimum (CBM), respectively. The Fermi level is set to 0 eV. (For interpretation of the references to colour in this figure legend, the reader is referred to the Web version of this article.)

vacancy-induced electronic structure modifications in the dilute limit [5].

The total density of states (TDOS) for the perfect and defective supercells is presented in Fig. 3. While pristine CdTe exhibits a clear band gap around the Fermi level ($E_F = 0$), the defective cases in panels **(b–f)** show small peaks and wiggles within this region. The introduction of a material defect into a perfect structure leads to the creation of localized modes within the band gap [74]. For the defective supercell, there are more electronic states near the band edges, likely due to the disruption of the periodic crystal structure caused by the defects. Panels **(e–f)** for the Te_{Cd} antisite show a more significant filling of the gap compared to vacancies. This indicates that antisites act as a deeper, more complex electronic traps that significantly perturb the host band's edges. In addition, introducing point defects creates additional states near the conduction-band edge and within the gap, indicating the perturbation of extended host states and partial electron localization. Consequently, the

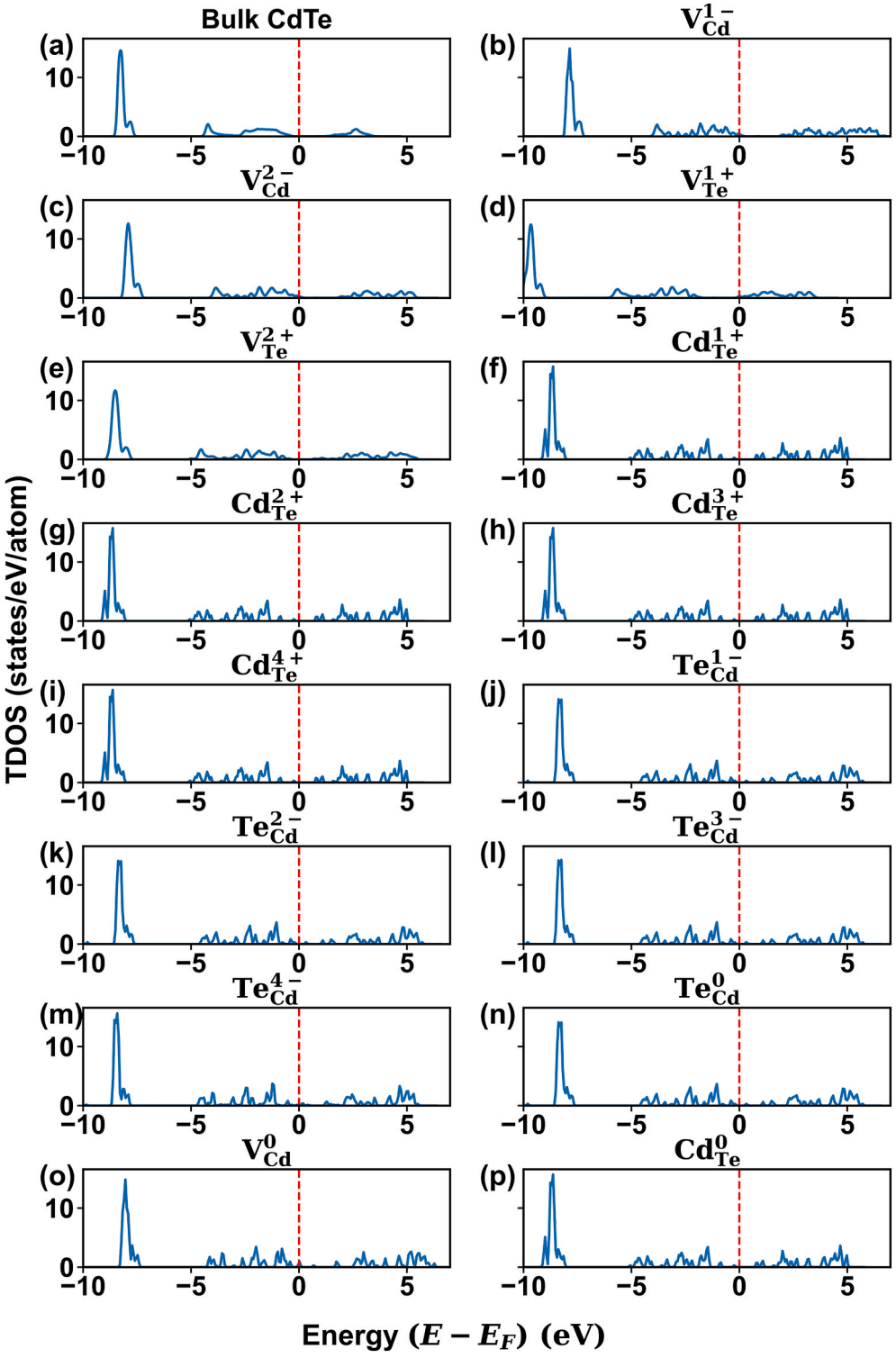

Fig. 3. Total density of states (TDOS) for bulk and defective CdTe. Panel **(a)** shows the 8-atom pristine cell, whereas panels **(b–p)** display 64-atom supercell containing different defective states. The Fermi level is set to 0 eV.

redistribution and broadening of states in the TDOS corroborate the trends observed in the band-structure analysis, confirming that the defect induced modifications are consistent across both electronic descriptions.

3.2. Stability and chemical potential

Fig. 4 shows the calculated chemical potentials of Cd and Te atoms for CdTe under various stoichiometric conditions. The x-axis represents the chemical potential of Cd (μ_{Cd}), while the y-axis represents the chemical potential of Te (μ_{Te}). The solid line labeled CdTe defines the thermodynamic phase boundary for the stability of CdTe, see equation (12).

This line separates Cd-rich and Te-rich growth conditions. The region below the line corresponds to Cd-rich conditions, where the chemical potential of Cd is relatively high and Cd-related defects or phases are thermodynamically favored. In contrast, the region above the line corresponds to Te-rich conditions, where the chemical potential of Te is higher and Te-related defects or phases are more stable.

Point A represents the Cd-rich limit, where the chemical potential of Cd reaches its maximum allowed value under equilibrium conditions ($\mu_{Cd} = 0\ eV$). At this point, the corresponding chemical potential of Te is – 0.90 eV, which is consistent with our calculated formation energy. Conversely, point B represents the Te-rich limit, where the chemical potential of Te is at its maximum ($\mu_{Te} = 0\ eV$), and the chemical potential of Cd is – 0.90 eV.

The line connecting points A and B represent the range of chemical potentials for which CdTe remains thermodynamically stable. The point labeled CdTe on this line indicates the equilibrium condition where CdTe coexists with its elemental constituents. To the right of the line (toward point A), the system becomes Cd-rich due to the higher chemical potential of Cd and lower chemical potential of Te, whereas to the left of the line (toward point B), the system becomes Te-rich because chemical potential of Te is higher relative to chemical potential of Cd.

The slope of the line is determined by the stoichiometry of CdTe. For every point along this line, the sum of the chemical potentials of Cd and Te equals the total formation energy of the CdTe phase. The equation of straight line CdTe as:

$$y = -x - 0.90309, \tag{12}$$

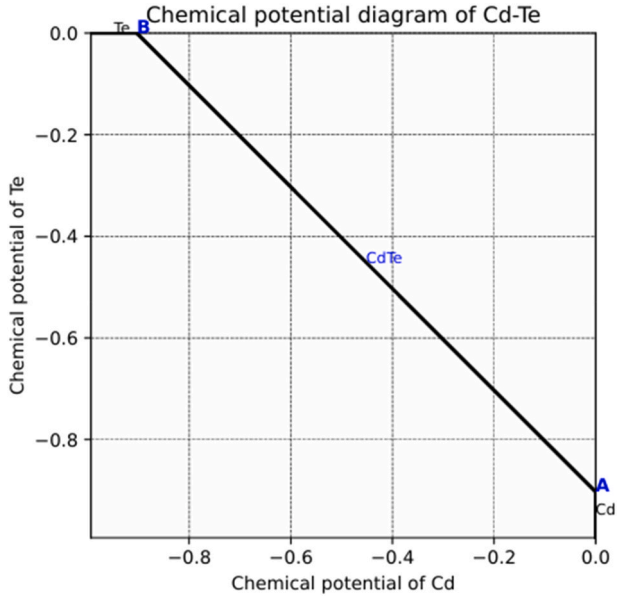

Fig. 4. The chemical potential diagram of CdTe. The units of both axes are in eV. Point A represents Cd-rich condition, and point B represent Te-rich condition.

where μ_i are bounded by $\mu_{Cd} \leq 0$, $\mu_{Te} \leq 0$ and μ_i are limited to those values that maintain a stable CdTe compound, so $\mu_{Cd} + \mu_{Te} = \Delta H_f(CdTe)$ and $\Delta H_f(CdTe) < \mu_{Te} < 0$, where $\Delta H_f(CdTe)$ is the formation energy of solid CdTe. $\Delta H_f(CdTe)$ is calculated to be – 0.90 eV, which is in reasonable agreement with the experimental values in the range from – 0.73 to – 0.96 eV [26].

To determine the Fermi level induced by intrinsic defects, appropriate growth conditions must be selected. Experimentally, these conditions depend on molecular precursor concentrations, while theoretically, they are defined by the chemical potentials (μ_{Cd}, μ_{Te}). In this work, we chose chemical potential values corresponding to ($\Delta\mu_{Cd}, \Delta\mu_{Te}$) of (– 0.903 eV), which ensures the thermodynamic stability of CdTe and provides a physically consistent framework for evaluating defects energetics.

3.3. Defect formation energies and electrical activity

We employed supercells containing 64 and 216 atoms to model intrinsic point defects in CdTe. In the present study we have studied 16 native point defects: Cd and Te vacancies (V_{Cd}, V_{Te}) and antisites (Cd_{Te}, Te_{Cd}) across various charge states. The formation energies of each defect are calculated as functions of the Fermi level ranging from the VBM to the theoretical band gap of 1.42 eV. The detailed formation energies obtained from our calculations are listed in Table 1. Fig. 5 presents these energies for the 216-atom supercell under different growth conditions, while the corresponding results for the 64-atom supercell are provided in Fig. S1 of the Supplementary information. For each intrinsic defect considered, only the charge state with the minimum formation energy at a given Fermi level is displayed. The slope of the line in the defect formation energy with respect to Fermi level reflects the charge-state dependence of the defect and identifies whether it behaves as a donor or an acceptor. A positive slope corresponds to donor-like behavior, whereas a negative slope indicates an acceptor-like behavior, consistent with established thermodynamic formalisms for defects in semiconductors [5,20,75].

The FNV electrostatic correction was applied to both the 64-atom and 216-atom supercells to reduce long-range electrostatic interactions in defect calculations. Although finite size corrections can reduce long-range electrostatic interactions in defect calculations, some residual supercell-size effects may remain due to short-range elastic interactions, artificial defect-state dispersion, and constrained structural relaxation in smaller supercells. These effects can influence both the local defect geometry and the calculated defect energetics, particularly for defects associated with significant lattice distortions and localized electronic states. Nevertheless, the comparison between the two

Table 1
Defect states and their formation energies in 64 atom and 216 atom CdTe supercells.

Defect Name	Atom I/O	Charge State	Formation Energy (eV)	
			64 Atom	216 Atom
Cd_{Te1}	Cd: 1 Te: −1	0	1.873	2.199
		1	1.223	1.564
		2	0.613	0.985
		3	0.685	0.950
		4	0.799	0.959
Te_{Cd1}	Te: 1 Cd: −1	−4	5.305	5.347
		−3	5.643	5.651
		−2	3.433	3.469
		−1	2.595	2.771
		0	1.803	2.126
Va_{Cd1}	Cd: −1	−2	2.299	2.567
		−1	2.233	2.473
		0	2.209	2.423
Va_{Te1}	Te: −1	0	1.655	1.925
		1	1.185	1.343
		2	0.760	0.817

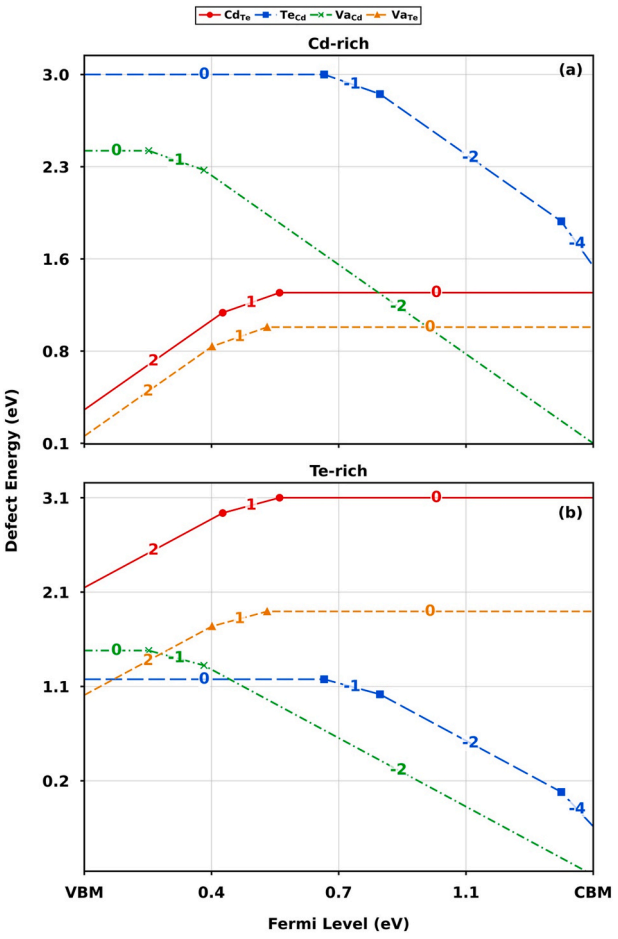

Fig. 5. Defect formation energy (eV) diagrams for a 216 atom CdTe supercell, presented under (a) Cd-rich and (b) Te-rich conditions, respectively.

supercell sizes provides valuable insight into the convergence behavior of the defect properties, while the larger 216-atom supercell generally provides a more reliable description of the isolated-defect limit by further reducing periodic image interactions and improving the convergence of structural and electronic properties.

3.3.1. *Cd-rich conditions*

Under Cd-rich conditions [Fig. 5 (a)], Cd_{Te} and V_{Te} exhibit positive slopes, identifying them as donor-type defects. As the Fermi level shifts toward the conduction band minimum (CBM), their formation energies increase, reflecting their tendency to lose electrons and become positively charged. These donors supply free electrons, thereby promoting n-type conductivity under Cd-rich growth environments.

Conversely, V_{Cd} possesses a negative slope, characterizing it as an acceptor. Its formation energy decreases with an increasing Fermi level, indicating a tendency to capture electrons and generate holes. However, under Cd rich conditions, V_{Cd} exhibits a relatively high formation energy, making it less energetically favorable than the dominant donor defects. While Te_{Cd} also displays acceptor-like behavior, its high formation energy across most of the Fermi-level range suggests a negligible contribution to p-type conductivity. Overall, the energetic prevalence of donor defects drives the intrinsic n-type behavior of CdTe under Cd-rich conditions, consistent with the defect thermodynamics observed for II-VI semiconductors [76–78].

3.3.2. *Te-rich conditions*

Under Te-rich growth conditions [Fig. 5 (b)], V_{Cd} and Te_{Cd} become significantly more energetically favorable while maintaining negative slopes, confirming their acceptor-like character. These defects act as acceptors by capturing electrons from the Fermi reservoir, thereby promoting p-type conductivity [12]. In contrast, Cd_{Te} and V_{Te} retain positive slopes consistent with donor behavior; however, their formation energies exceed those of the acceptor species across most of the Fermi-level range. As a result, donor defects are less likely to form under Te-rich conditions. This redistribution of defect stability explains the enhanced tendency toward p-type conductivity in Te-rich CdTe, where the lower formation energy of acceptors dictates the dominant carrier type.

3.3.3. *Implications for carrier transport and device performance*

The defect formation energy diagrams illustrate two primary performance bottlenecks in CdTe: self-compensation and carrier recombination. As the Fermi level moves toward the band edges to increase the conductivity, the formation energy of opposing defects -such as V_{Te} in p-type or V_{Cd} in n-type material decreases sharply. This leads to the spontaneous creation of compensating defects that neutralize free carriers and pin the Femi level. Furthermore, the kinks in the formation energy line for anti-sites, such as Te_{Cd} represent deep-level transition states that act as potent recombination centers. These traps capture charge carriers and dissipation of their energy, drastically reducing minority carrier lifetimes and mobility, which limits the open-circuit voltage (V_{OC}) and the overall efficiency of the device [79].

3.4. *Photoluminescence (PL) spectra and optical activity*

The PL spectra and phonon spectral function for various defect states in the 64-atom CdTe supercell are presented in Fig. 6. These calculations were performed using PBEsol functional since HSE06 calculations for large supercells are computationally too expensive. Each subplot provides two primary types of information for each defect: the spectral distribution of the Huang-Rhys factor, S ($\hbar\omega$) (left), and the simulated PL intensity relative to the zero-phonon line (E_{ZPL}) (right). The results reveal a clear dichotomy between vacancy-type defects and antisites regarding their optical signatures. The discrete phonon modes in each panel are indicated by the red vertical bars. The spectral function S ($\hbar\omega$) for electron-phonon coupling was calculated according to Equation (6) in the Methods section.

For all configurations, the energy of zero phonon line (E_{ZPL}) was set to 2600 meV. The results demonstrate that the HR factor (S) varies significantly across different defect states, as detailed below.

1. Tellurium Vacancy (V_{Te}) states
   Panels **(a)** and **(b)** represent the tellurium vacancy in its neutral (V_{Te}^{0}) and charged (V_{Te}^{2+}) states, respectively. Both configurations exhibit spectral peaks around 10 meV. However, the total HR factor is notably higher for the charged state (S = 15.19) compared to the neutral state (S = 4.84). This indicates stronger electron-phonon coupling in the charged state, likely due to increased lattice distortion. The simulated PL intensity for the charged state is characterized by a broader profile and a peak shift of approximately 100 meV, whereas the neutral state shifts by only ~ 50 meV.
2. Neutral Cadmium Vacancy (V_{Cd}^{0})
   Panel **(c)** depicts the neutral cadmium vacancy, where peak emerges at an energy of approximately 20 meV. This configuration exhibits negligible electron-phonon coupling (S = 0.0024). As a result, the simulated PL intensity features an extremely sharp peak centered exactly at the $E - E_{ZPL} = 0$. This indicates a weak electron phonon coupling typical of a shallow state that does not significantly perturb the surrounding crystal lattice.
3. Neutral Tellurium Antisite (Te_{Cd}^{0})
   Panel **(d)** represents the neutral tellurium antisite. In this case, two distinct peaks appear around 10 meV and 20 meV, distributed across both acoustic and optical phonon modes. This configuration shows

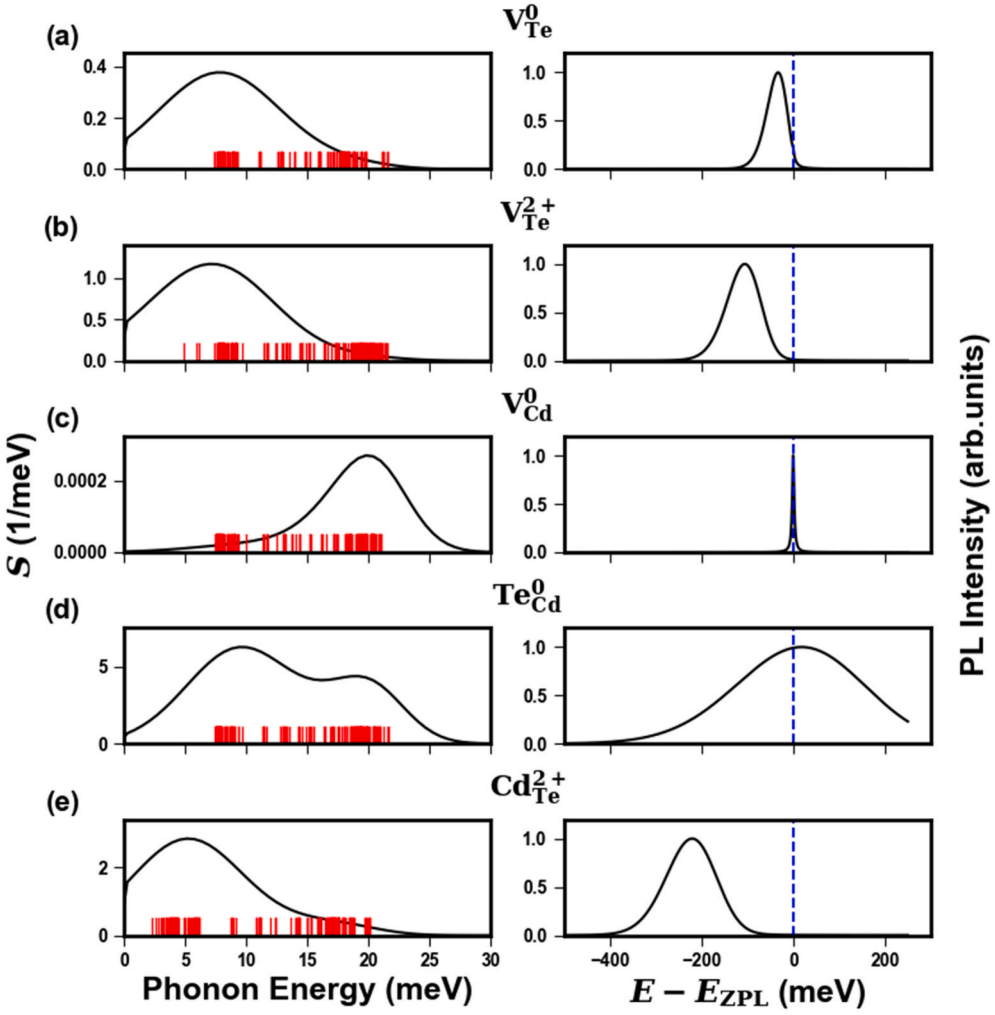

Fig. 6. Spectral density function S ($\hbar\omega$) and corresponding photoluminescence (PL) spectra for intrinsic point defects in CdTe. Vertical red lines mark phonon modes, while the dashed line at $E - E_{ZPL} = 0$ denotes the zero-phonon line (ZPL). The defective configurations and their charge states are shown in the panels (a), (b), (c), (d), and (e) respectively. (For interpretation of the references to colour in this figure legend, the reader is referred to the Web version of this article.)

intense electron-phonon coupling (S = 100.07), resulting in a significant degree of lattice distortion. The resulting PL line shape is a broad, Gaussian-like curve, underscoring that the coupling strength correlates with spectral broadening.

4. Ionized Cadmium Antisite (Cd_{Te}^{2+})

Panel **(e)** displays the ionized cadmium antisite. Here, the peak occurs at approximately 5 meV with a total HR factor of S = 35.55. This configuration exhibits the most dramatic Franck-Condon shift, with the emission peak centered nearly 200 meV.

The calculated HR factors may be affected by elastic-finite size effects associated with the 64-atom supercell, as defect-induced lattice distortions can interact with their periodic images and modify the long-range relaxation behavior. Since HR factor is directly related to the lattice displacement during the optical transition, it is expected to be more sensitive to finite-size effects than the overall PL line shape. Previous first-principles studies have shown that HR factors exhibit noticeable supercell-size dependence, whereas the corresponding PL spectra remain comparatively less sensitive and still retain the main spectral features after finite-size corrections [31]. Therefore, although the absolute HR values reported here should be regarded as approximate, the predicted PL spectra trends and qualitative defect-emission characteristics are expected to remain physically meaningful.

The spectral densities further show that the dominant phonon contributions occur mainly in the low energy phonon region (∼ 5–22 meV), indicating strong defect-phonon interactions. These findings are in good agreement with the experimental CdTe PL study by Furstenberg and White [80], where broadened defect-band emission, pronounced longitudinal optical (LO) phonon replicas, and large HR factors were associated with significant lattice distortion. Thus, our theoretical analysis reveals that the optical signature of a defect is determined by its interaction with the crystal lattice. Neutral vacancies, such as (V_{Cd}^{0}) exhibit weak phonon coupling, resulting in sharp, zero phonon line dominating emission characteristic of shallow states. Conversely, antisite defects (Te_{Cd}, Cd_{Te}) create deep levels with strong phonon coupling producing broad Gaussian PL profiles. So, these results suggest that vacancies typically produce sharp PL spectra while antisite defects result in broad, deep bands and distort the lattice much more aggressively than simple vacancies.

4. Conclusion

In this study, we systematically investigated the electronic properties, intrinsic point defects, and defect formation energy diagrams of CdTe using density functional theory calculations with 64 and 216-atom supercells. Furthermore, PL line shapes were simulated for the defect systems within the 64-atom supercell. We studied the lattice constants and CPD diagram, as presented in Fig. 1. Our calculated lattice constant

of 6.60 Å is approximately 2% larger than values observed in previous experimental studies [81]. Analysis of the band structures and total density of states for both pristine and defective CdTe demonstrates that defects significantly perturb the electronic structure, inducing localized states and band splitting near the Fermi level. Additionally, shifts in the band extrema to different k-points indicate modifications to the band gap. Vacancies and antisites are identified as the most prevalent native defects. To the best of our knowledge, first-principles studies of PL spectra in CdTe are still lacking. Our results reveal that neutral vacancy defects exhibit sharp emission dominated by the zero-phonon line, resulting in weak electron-phonon coupling. In contrast, antisite defects introduce deep transition levels that lead to strong electron phonon interactions and broad PL spectra. These findings demonstrate that the optical quality of CdTe is governed by the specific nature of the dominant defect species.

Disclaimer

The views and conclusions contained herein are those of authors and should not be interpreted as necessarily representing the official policies or endorsements, either expressed or implied, of Air Force Research Laboratory or the U.S. Government.

CRediT authorship contribution statement

M. Sitaula: Investigation, Methodology, Software, Validation, Visualization, Writing – original draft, Writing – review & editing. **V.T. Barone:** Methodology, Software, Writing – review & editing. **B. K C:** Methodology, Software, Writing – review & editing. **B.R. Tuttle:** Writing – review & editing. **R.J. Ellingson:** Conceptualization, Funding acquisition, Project administration. **S.V. Khare:** Conceptualization, Funding acquisition, Project administration, Resources, Supervision, Writing – review & editing.

Declaration of competing interest

The authors declare that they have no known competing financial interests or personal relationships that could have appeared to influence the work reported in this paper.

Acknowledgements

This material is based on research sponsored by the Air Force Research Laboratory (AFRL) under Agreement No. FA9453-19-C-1002. The U.S. Government is authorized to reproduce and distribute reprints for Governmental purposes not withstanding any copyright notation thereon. The views expressed are those of the authors and do not reflect the official guidance or position of the United States Government, the Department of Defense or of the United States Air Force. The appearance of external hyperlinks does not constitute endorsement by the United States Department of Defense (DoD) of the linked websites, or the information, products, or services contained therein. The Dod does not exercise any editorial, security, or other control over the information you may find at these locations. Approved for public release; distribution is unlimited.

The calculations for this research were conducted at the University of Toledo computing clusters.

Appendix A. Supplementary data

Supplementary data to this article can be found online at https://doi.org/10.1016/j.solmat.2026.114514.

Data availability

Data will be made available on request.

References

[1] A.L. Fahrenbruch, R.H. Bube, Fundamentals of Solar Cells: Photovoltaic Solar Energy Conversion, first ed., Elsevier, 2012.
[2] B.E. McCandless, J.R. Sites, Cadmium telluride solar cells, in: Handbook of Photovoltaic Science and Engineering, 2011, pp. 600–641, https://doi.org/10.1002/9780470974704.
[3] J. Zázvorka, P. Hlídek, R. Grill, J. Franc, E. Belas, Photoluminescence of CdTe: in the spectral range around 1.1 eV, J. Lumin. 177 (2016) 71–81, https://doi.org/10.1016/j.jlumin.2016.04.019.
[4] S. Kodambaka, V. Petrova, S. Khare, D. Gall, A. Rockett, I. Petrov, J. Greene, Size-dependent detachment-limited decay kinetics of two-dimensional TiN Islands on TiN (111), Phys. Rev. Lett. 89 (2002) 176102, https://doi.org/10.1103/PhysRevLett.89.176102.
[5] C. Freysoldt, B. Grabowski, T. Hickel, J. Neugebauer, G. Kresse, A. Janotti, C. G. Van de Walle, First-principles calculations for point defects in solids, Rev. Mod. Phys. 86 (2014) 253–305, https://doi.org/10.1103/RevModPhys.86.253.
[6] H.-S. Zhang, L. Shi, Z.-H. Liu, G.-Z. Xu, W.-T. Song, Y.-K. Wang, Z.-J. Xu, X.-B. Yang, Y.-J. Zhao, X.-L. Yang, Theoretical simulation and experimental verification of the competition between different recombination channels in GaN semiconductors, J. Mater. Chem. C 10 (2022) 13191–13200, https://doi.org/10.1039/D2TC02164A.
[7] J.-J. Kang, F.-J. Kang, S.-S. Liu, Z. Peng, Y.-H. Cheng, H.-S. Zhang, The impact of IGe defects on the photovoltaic performance of $CsGeI_3$: a DFT and NAMD study, Sol. Energy Mater. Sol. Cell. 295 (2026) 113988, https://doi.org/10.1016/j.solmat.2025.113988.
[8] I. Mosquera-Lois, S.R. Kavanagh, A. Walsh, D.O. Scanlon, Identifying the ground state structures of point defects in solids, npj Comput. Mater. 9 (2023) 25, https://doi.org/10.1038/s41524-023-00973-1.
[9] S. Kodambaka, S. Khare, W. Święch, K. Ohmori, I. Petrov, J. Greene, Dislocation-driven surface dynamics on solids, Nature 429 (2004) 49–52, https://doi.org/10.1038/nature02531.
[10] J.-H. Yang, W.-J. Yin, J.-S. Park, J. Ma, S.-H. Wei, Review on first-principles study of defect properties of CdTe as a solar cell absorber, Semicond. Sci. Technol. 31 (2016) 083002, https://doi.org/10.1088/0268-1242/31/8/083002.
[11] A. Castaldini, A. Cavallini, B. Fraboni, P. Fernandez, J. Piqueras, Deep energy levels in CdTe and CdZnTe, J. Appl. Phys. 83 (1998) 2121–2126, https://doi.org/10.1063/1.366946.
[12] S.R. Kavanagh, A. Walsh, D.O. Scanlon, Rapid recombination by cadmium vacancies in CdTe, ACS Energy Lett. 6 (2021) 1392–1398, https://doi.org/10.1021/acsenergylett.1c00380.
[13] N. Jiang, J.L. Roehl, S.V. Khare, D.G. Georgiev, A.H. Jayatissa, An ab initio computational study of pure Zn_3N_2 and its native point defects and dopants Cu, Ag and Au, Thin Solid Films 564 (2014) 331–338, https://doi.org/10.1016/j.tsf.2014.05.032.
[14] S. Chaulagain, E. Amonette, M.K. Mainali, P. Dulal, A.V. Bordovalos, Z. Song, N. J. Podraza, Complex optical properties of single crystal and atomic layer deposited alumina from the terahertz to vacuum ultraviolet spectral range, J. Appl. Phys. 139 (2026), https://doi.org/10.1063/5.0314998.
[15] P. Dulal, M.K. Mainali, S. Chaulagain, B. Shrestha, E. Amonette, A. Shan, N. J. Podraza, Optical properties of fused silica glass using spectroscopic ellipsometry from 0.4 meV to 8.5 eV, Surf. Sci. Spectra 32 (2025) 026001, https://doi.org/10.1116/6.0004538.
[16] Y.-T. Huang, S.R. Kavanagh, D.O. Scanlon, A. Walsh, R.L. Hoye, Perovskite-inspired materials for photovoltaics and beyond—from design to devices, Nanotechnology 32 (2021) 132004, https://doi.org/10.1088/1361-6528/abcf6d.
[17] Z. Li, S.R. Kavanagh, M. Napari, R.G. Palgrave, M. Abdi-Jalebi, Z. Andaji-Garmaroudi, D.W. Davies, M. Laitinen, J. Julin, M.A. Isaacs, Bandgap lowering in mixed alloys of $Cs_2Ag(Sb_xBi_{1-x})Br_6$ double perovskite thin films, J. Mater. Chem. A 8 (2020) 21780–21788, https://doi.org/10.1039/D0TA07145E.
[18] U. Rau, B. Blank, T.C. Müller, T. Kirchartz, Efficiency potential of photovoltaic materials and devices unveiled by detailed-balance analysis, Phys. Rev. Appl. 7 (2017) 044016, https://doi.org/10.1103/PhysRevApplied.7.044016.
[19] M.A. Green, Radiative efficiency of state-of-the-art photovoltaic cells, Prog. Photovoltaics Res. Appl. 20 (2012) 472–476, https://doi.org/10.1002/pip.1147.
[20] S. Zhang, J.E. Northrup, Chemical potential dependence of defect formation energies in GaAs: application to Ga self-diffusion, Phys. Rev. Lett. 67 (1991) 2339, https://doi.org/10.1103/PhysRevLett.67.2339.
[21] S. Lany, A. Zunger, Assessment of correction methods for the band-gap problem and for finite-size effects in supercell defect calculations: case studies for ZnO and GaAs, Phys. Rev. B Condens. Matter 78 (2008) 235104, https://doi.org/10.1103/PhysRevB.78.235104.
[22] C. Freysoldt, J. Neugebauer, C.G. Van de Walle, Fully ab initio finite-size corrections for charged-defect supercell calculations, Phys. Rev. Lett. 102 (2009) 016402, https://doi.org/10.1103/PhysRevLett.102.016402.
[23] C. Freysoldt, J. Neugebauer, C.G. Van de Walle, Electrostatic interactions between charged defects in supercells, Phys. Status Solidi 248 (2011) 1067–1076, https://doi.org/10.1002/pssb.201046289.
[24] Y. Kumagai, F. Oba, Electrostatics-based finite-size corrections for first-principles point defect calculations, Phys. Rev. B 89 (2014) 195205, https://doi.org/10.1103/PhysRevB.89.195205.
[25] E. Menéndez-Proupin, W. Orellana, Theoretical study of intrinsic defects in CdTe, J. Phys. Conf. 720 (2016) 012031, https://doi.org/10.1088/1742-6596/720/1/012031. IOP Publishing.

[26] S.-H. Wei, S. Zhang, Chemical trends of defect formation and doping limit in II-VI semiconductors: the case of CdTe, Phys. Rev. B 66 (2002) 155211, https://doi.org/10.1103/PhysRevB.66.155211.

[27] C.W. Castleton, A. Höglund, S. Mirbt, Managing the supercell approximation for charged defects in semiconductors: Finite-size scaling, charge correction factors, the band-gap problem, and the ab initio dielectric constant, Phys. Rev. B Condens. Matter 73 (2006) 035215, https://doi.org/10.1103/PhysRevB.73.035215.

[28] A. Alkauskas, P. Broqvist, A. Pasquarello, Defect energy levels in density functional calculations: alignment and band gap problem, Phys. Rev. Lett. 101 (2008) 046405, https://doi.org/10.1103/PhysRevLett.101.046405.

[29] P. Gunaicha, S. Gangam, J. Roehl, S. Khare, Structural, energetic and elastic properties of $Cu_2ZnSn(S_xSe_{1-x})_4$ (x = 1, 0.75, 0.5, 0.25, 0) alloys from first-principles computations, Sol. Energy 102 (2014) 276–281, https://doi.org/10.1016/j.solener.2014.01.015.

[30] S. Kandel, B. Dumre, D. Gall, S. Khare, Prediction of super hardness in transition metal hexa-nitrides from density functional theory computations, Materialia 25 (2022) 101550, https://doi.org/10.1016/j.mtla.2022.101550.

[31] Y. Jin, M. Govoni, G. Wolfowicz, S.E. Sullivan, F.J. Heremans, D.D. Awschalom, G. Galli, Photoluminescence spectra of point defects in semiconductors: validation of first-principles calculations, Phys. Rev. Mater. 5 (2021) 084603, https://doi.org/10.1103/PhysRevMaterials.5.084603.

[32] K. Huang, A. Rhys, Theory of light absorption and non-radiative transitions in F-centres, Proc. R. Soc. Lond., Ser. A Math. Phys. Sci. 204 (1950) 406–423, https://doi.org/10.1098/rspa.1950.0184.

[33] S.A. Tawfik, S.P. Russo, PyPhotonics: a python package for the evaluation of luminescence properties of defects, Comput. Phys. Commun. 273 (2022) 108222, https://doi.org/10.1016/j.cpc.2021.108222.

[34] R. Kubo, Y. Toyozawa, Application of the method of generating function to radiative and non-radiative transitions of a trapped electron in a crystal, Prog. Theor. Phys. 13 (1955) 160–182, https://doi.org/10.1143/PTP.13.160.

[35] A. Alkauskas, B.B. Buckley, D.D. Awschalom, C.G. Van de Walle, First-principles theory of the luminescence lineshape for the triplet transition in diamond NV centres, New J. Phys. 16 (2014) 073026, https://doi.org/10.1088/1367-2630/16/7/073026.

[36] M. Berding, Native defects in CdTe, Phys. Rev. B 60 (1999) 8943, https://doi.org/10.1103/PhysRevB.60.8943.

[37] S. Kodambaka, V. Petrova, S. Khare, D.D. Johnson, I. Petrov, J. Greene, Absolute TiN (111) step energies from analysis of anisotropic island shape fluctuations, Phys. Rev. Lett. 88 (2002) 146101, https://doi.org/10.1103/PhysRevLett.88.146101.

[38] D.V. Dinh, X. Lü, O. Brandt, D. Sen, O. Fairlamb, F. Peiris, F. Lima, A. Bordovalos, S. Chaulagain, A. Shan, Reststrahlen band and optical bandgaps in semiconducting CrN films, Phys. Rev. Mater. 10 (2026) 044602, https://doi.org/10.1103/gt8b-1psw.

[39] G. Kresse, J. Hafner, Ab initio molecular dynamics for liquid metals, Phys. Rev. B 47 (1993) 558, https://doi.org/10.1103/PhysRevB.47.558.

[40] G. Kresse, J. Furthmüller, Efficiency of ab-initio total energy calculations for metals and semiconductors using a plane-wave basis set, Comput. Mater. Sci. 6 (1996) 15–50, https://doi.org/10.1016/0927-0256(96)00008-0.

[41] G. Kresse, J. Furthmüller, Efficient iterative schemes for ab initio total-energy calculations using a plane-wave basis set, Phys. Rev. B 54 (1996) 11169, https://doi.org/10.1103/PhysRevB.54.11169.

[42] M. Sitaula, V. Barone, S. Kandel, B. Kc, B. Dumre, R. Ellingson, S. Khare, Optoelectronic and mechanical properties of antimony sulfide selenide ternary $Sb_2(S_xSe_{1-x})_3$ alloys using first principles methods, Comput. Condens. Matter (2025) e01103, https://doi.org/10.1016/j.cocom.2025.e01103.

[43] L.-L. Wang, S.V. Khare, V. Chirita, D.D. Johnson, A.A. Rockett, A.I. Frenkel, N. H. Mack, R.G. Nuzzo, Origin of bulklike structure and bond length disorder of Pt37 and Pt6Ru31 clusters on carbon: comparison of theory and experiment, J. Am. Chem. Soc. 128 (2006) 131–142, https://doi.org/10.1021/ja053896m.

[44] J.P. Perdew, J. Chevary, S. Vosko, K.A. Jackson, M.R. Pederson, D. Singh, C. Fiolhais, Erratum: atoms, molecules, solids, and surfaces: applications of the generalized gradient approximation for exchange and correlation, Phys. Rev. B 48 (1993) 4978, https://doi.org/10.1103/PhysRevB.46.6671.

[45] J.P. Perdew, J.A. Chevary, S.H. Vosko, K.A. Jackson, M.R. Pederson, D.J. Singh, C. Fiolhais, Atoms, molecules, solids, and surfaces: applications of the generalized gradient approximation for exchange and correlation, Phys. Rev. B 46 (1992) 6671, https://doi.org/10.1103/PhysRevB.46.6671.

[46] B. Kc, V. Barone, S. Kandel, M. Sitaula, B. Dumre, R. Ellingson, S. Khare, Computational investigation of structural, electronic, and optical properties of $(In_xGa_{1-x})_2O_3$ alloys as candidates for emitter layer application in solar cells, Phys. B Condens. Matter (2025) 417615, https://doi.org/10.1016/j.physb.2025.417615.

[47] S. Kandel, D. Gall, S. Khare, Density functional theory calculations of mechanical and electronic properties of $W_{1-x}Ta_xN_6$, $W_{1-x}Mo_xN_6$, and $Mo_{1-x}Ta_xN_6$ ($0 \leq x \leq 1$) alloys in a hexagonal structure, J. Vac. Sci. Technol. A 41 (2023), https://doi.org/10.1116/6.0002923.

[48] G. Kresse, D. Joubert, From ultrasoft pseudopotentials to the projector augmented-wave method, Phys. Rev. B 59 (1999) 1758, https://doi.org/10.1103/PhysRevB.59.1758.

[49] P.E. Blöchl, Projector augmented-wave method, Phys. Rev. B 50 (1994) 17953, https://doi.org/10.1103/PhysRevB.50.17953.

[50] J. Roehl, Z. Liu, S. Khare, Diffusion in CdS of Cd and S vacancies and Cu, Cd, Cl, S and Te interstitials studied with first-principles computations, Mater. Res. Express 1 (2014) 025904, https://doi.org/10.1088/2053-1591/1/2/025904.

[51] N. Szymanski, I. Khatri, J. Amar, D. Gall, S. Khare, Unconventional superconductivity in 3d rocksalt transition metal carbides, J. Mater. Chem. C 7 (2019) 12619–12632, https://doi.org/10.1039/C9TC03793D.

[52] Y. Wang, Z.T. Liu, S.V. Khare, S.A. Collins, J. Zhang, L. Wang, Y. Zhao, Thermal equation of state of silicon carbide, Appl. Phys. Lett. 108 (2016), https://doi.org/10.1063/1.4941797.

[53] A.V. Krukau, O.A. Vydrov, A.F. Izmaylov, G.E. Scuseria, Influence of the exchange screening parameter on the performance of screened hybrid functionals, J. Chem. Phys. 125 (2006), https://doi.org/10.1063/1.2404663.

[54] N. Szymanski, V. Adhikari, M. Willard, P. Sarin, D. Gall, S. Khare, Prediction of improved magnetization and stability in $Fe_{16}N_2$ through alloying, J. Appl. Phys. 126 (2019), https://doi.org/10.1063/1.5109571.

[55] B. Kc, M. Sitaula, V. Barone, S. Kandel, S. Khare, Opto-electronic and mechanical properties of $(Cd_x\ Zn_{1-x})_2SnO_4$ in the cubic and orthorhombic phases using first-principles methods, J. Appl. Phys. 139 (2026), https://doi.org/10.1063/5.0316837.

[56] S. Kandel, B. Dumre, D. Gall, S. Khare, Mechanical and electronic properties of transition metal hexa-nitrides in hexagonal structure from density functional theory calculations, Comput. Mater. Sci. 221 (2023) 112084, https://doi.org/10.1016/j.commatsci.2023.112084.

[57] A.V. Terentjev, L.A. Constantin, J.M. Pitarke, Dispersion-corrected PBEsol exchange-correlation functional, Phys. Rev. B 98 (2018) 214108, https://doi.org/10.1103/PhysRevB.98.214108.

[58] Y. Kumagai, N. Tsunoda, A. Takahashi, F. Oba, Insights into oxygen vacancies from high-throughput first-principles calculations, Phys. Rev. Mater. 5 (2021) 123803, https://doi.org/10.1103/PhysRevMaterials.5.123803.

[59] J. Ren, G. Bian, L. Fu, C. Liu, T. Wang, G. Zha, W. Jie, M. Neupane, T. Miller, M. Hasan, Electronic structure of the quantum spin Hall parent compound CdTe and related topological issues, Phys. Rev. B 90 (2014) 205211, https://doi.org/10.1103/PhysRevB.90.205211.

[60] X. Xiang, Y. Tong, A. Gehrke, S.T. Dunham, Point defects in CdTe and CdTeSe alloy: a first principles investigation with DFT+ U, Phys. Rev. Mater. 8 (2024) 084602, https://doi.org/10.1103/PhysRevMaterials.8.084602.

[61] B.R. Tuttle, E.J. Payne, Z.J. Willard, S.V. Khare, V. Pecunia, Atomic theory of point defect assisted carrier recombination in $Rb_3Sb_2I_9$, J. Phys. Chem. Solid. (2025) 113190, https://doi.org/10.1016/j.jpcs.2025.113190.

[62] S. Khare, T. Einstein, Energetics of steps and kinks on Ag and Pt using equivalent crystal theory (ECT), Surf. Sci. 314 (1994) L857–L865, https://doi.org/10.1016/0039-6028(94)90207-0.

[63] S. Kandel, B. Dumre, D. Gall, S. Khare, Investigation of hardness in transition metal hexa-nitrides in cubic structure: a first-principles study, J. Phys. Chem. Solid. 171 (2022) 111022, https://doi.org/10.1016/j.jpcs.2022.111022.

[64] J.L. Lyons, C.G. Van de Walle, Computationally predicted energies and properties of defects in GaN, npj Comput. Mater. 3 (2017) 12, https://doi.org/10.1038/s41524-017-0014-2.

[65] M.H. Rahman, S. Rojsatien, D. Krasikov, M.K. Chan, M. Bertoni, A. Mannodi-Kanakkithodi, First principles investigation of dopants and defect complexes in $CdSe_xTe_{1-x}$, Sol. Energy Mater. Sol. Cell. 293 (2025) 113857, https://doi.org/10.1016/j.solmat.2025.113857.

[66] A. Hashemi, C. Linderälv, A.V. Krasheninnikov, T. Ala-Nissila, P. Erhart, H.-P. Komsa, Photoluminescence line shapes for color centers in silicon carbide from density functional theory calculations, Phys. Rev. B 103 (2021) 125203, https://doi.org/10.1103/PhysRevB.103.125203.

[67] A. Togo, I. Tanaka, First principles phonon calculations in materials science, Scr. Mater. 108 (2015) 1–5, https://doi.org/10.1016/j.scriptamat.2015.07.021.

[68] T. Miyakawa, D. Dexter, Phonon sidebands, multiphonon relaxation of excited states, and phonon-assisted energy transfer between ions in solids, Phys. Rev. B 1 (1970) 2961, https://doi.org/10.1103/PhysRevB.1.2961.

[69] J.J. Markham, Interaction of normal modes with electron traps, Rev. Mod. Phys. 31 (1959) 956, https://doi.org/10.1103/RevModPhys.31.956.

[70] K. Momma, F. Izumi, VESTA 3 for three-dimensional visualization of crystal, volumetric and morphology data, Appl. Crystallography 44 (2011) 1272–1276, https://doi.org/10.1107/S0021889811038970.

[71] A. Merad, M. Kanoun, G. Merad, J. Cibert, H. Aourag, Full-potential investigation of the electronic and optical properties of stressed CdTe and ZnTe, Mater. Chem. Phys. 92 (2005) 333–339, https://doi.org/10.1016/j.matchemphys.2004.10.031.

[72] G. Zeng, J. Zhang, W. Wang, L. Feng, Correlation of interfacial transportation properties of CdS/CdTe heterojunction and performance of CdTe polycrystalline thin-film solar cells, Int. J. Photoenergy 2015 (2015) 519386, https://doi.org/10.1155/2015/519386.

[73] J. Wang, G. Tang, X. Wu, M. Gu, Stable structure and effects of sulfur in CdTe/CdS heterojunctions, Surf. Interface Anal. 44 (2012) 434–438, https://doi.org/10.1002/sia.3822.

[74] A. Ezzarfi, F.Z. Elamri, F.Z. Safi, Y. Bouchafra, Y. Ben-Ali, A. Sali, D. Bria, High quality factor multichannel filter of electrons based on defective CdMnTe/CdTe multi-quantum wells, Phys. Scripta 96 (2021) 125811, https://doi.org/10.1088/1402-4896/ac217f.

[75] C.G. Van de Walle, J. Neugebauer, First-principles calculations for defects and impurities: applications to III-nitrides, J. Appl. Phys. 95 (2004) 3851–3879, https://doi.org/10.1063/1.1682673.

[76] A. Zunger, in: Practical Doping Principles, National Renewable Energy Lab.(NREL), Golden, CO (United States), 2003.

[77] S. Lany, A. Zunger, Anion vacancies as a source of persistent photoconductivity in II-VI and chalcopyrite semiconductors, Phys. Rev. B Condens. Matter 72 (2005) 035215, https://doi.org/10.1103/PhysRevB.72.035215.

[78] S. Lany, Semiconductor thermochemistry in density functional calculations, Phys. Rev. B Condens. Matter 78 (2008) 245207, https://doi.org/10.1103/PhysRevB.78.245207.

[79] M. Isah, C. Doroody, K.S. Rahman, M.N.A. Rahman, A.A. Goje, M.E.M. Soudagar, T. S. Kiong, N.M. Mubarak, A.W.M. Zuhdi, Exploring the impact of defect energy levels in CdTe/Si dual-junction solar cells using wxAMPS, Sci. Rep. 14 (2024) 4804, https://doi.org/10.1038/s41598-024-55616-2.

[80] R. Furstenberg, J.O. White, Photoluminescence study of the 1.3–1.55 eV defect band in CdTe, J. Cryst. Growth 305 (2007) 228–236, https://doi.org/10.1016/j.jcrysgro.2007.03.048.

[81] A. Aydinli, A. Compaan, G. Contreras-Puente, A. Mason, Polycrystalline $Cd_{1-x}Zn_xTe$ thin films on glass by pulsed laser deposition, Solid State Commun. 80 (1991) 465–468, https://doi.org/10.1016/0038-1098(91)90051-V.